# Energetics of Water Oxidation Catalyzed by Cobalt Oxide Nanoparticles: Assessing the Accuracy of DFT and DFT+U Approaches against Coupled Cluster Methods

Karolina Kwapien, Simone Piccinin, and Stefano Fabris*

CNR-IOM DEMOCRITOS Simulation Center, Istituto Officina dei Materiali, and SISSA, Via Bonomea 265, I-34136 Trieste, Italy

S  *Supporting Information*

**ABSTRACT:** Some of the most promising catalysts for water oxidation rely on crystalline and amorphous cobalt oxide nanoparticles. Density functional theory (DFT) calculations are routinely used to study the electronic and atomic structures of these materials as well as the thermodynamics and mechanisms of the electrochemical oxygen evolution reaction. The accuracy of these theoretical predictions has never been compared to high-level quantum chemistry methods. We perform coupled cluster (CC) quantum chemistry calculations on model cobalt oxide surface sites and use them to benchmark the accuracy of the most popular exchange and correlation functionals. Hybrid B3LYP and PBE0 functionals lead to fair agreement with the CC energies, while standard gradient-corrected functionals show important discrepancies. The inclusion of on-site electronic repulsion (DFT +U) substantially improves the calculated electronic and structural properties, but no value of the U parameter reproduces the CC results. We discuss the implications of these findings for amorphous cobalt phosphate nanoparticles, showing that the reactivity of these catalysts is not altered by surface phosphate groups.

**SECTION:** Surfaces, Interfaces, Porous Materials, and Catalysis
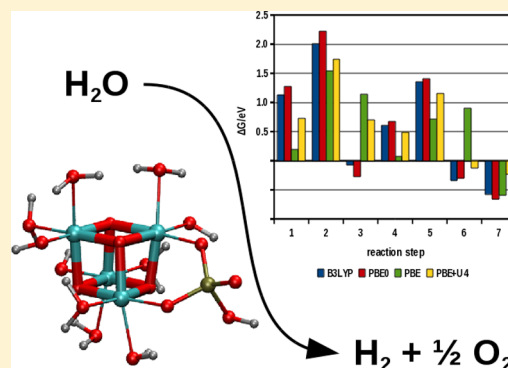
The lack of cheap and efficient materials that promote photoelectrochemical water splitting is currently one of the main limiting factors for the conversion and storage of solar energy.[1] The oxygen evolution reaction (OER) is the most challenging part of water splitting. It can be successfully catalyzed by materials based on noble metals like Ru, Ir, and Pt, but their scarcity and high prices have prompted a search for alternative materials based on more abundant elements.[2,3]

Among these, several Co oxides have been shown to offer a suitable balance between reactivity, structural stability, and resistance in the highly oxidative chemical environment of the OER. Examples include crystalline Co oxides ($Co_2O_3$, $Co_3O_4$, CoOOH),[4–8] perovskites,[9] as well as the recently discovered cobalt borate or cobalt phosphate (CoPi) amorphous materials.[3,10,11] The latter have been shown to be particularly promising due to both their ability to promote the OER at neutral pH with low electrochemical overpotential and their structural resistance and self-repairing capability under reaction conditions.[12–15]

Computational studies based on density functional theory (DFT) have been used to investigate the reaction thermodynamics of Co-based catalysts. The general problem with such an approach is that the standard local density (LDA) and gradient-corrected (GGA) approximations used in DFT for the exchange and correlation functionals often fail to describe the electronic properties of transition-metal oxides. Reaction

energies calculated with these approaches therefore require particular consideration.

For the case of extended crystalline $Co_3O_4$ surfaces, this issue has been analyzed in detail by Chen and Selloni, who combined GGA, hybrid PBE0 functionals, and DFT+U approaches.[4,5] The latter method was also used to study the energetics of water oxidation at Co oxide surfaces.[6,8,16] The DFT+U approach is appealing because it rectifies the major shorcoming of LDA/GGA functionals for transition-metal oxides with a fraction of the computational resources required by hybrid functional calculations. Notably, the method relies on the choice of specific values of the parameter U and of the projectors used to define the on-site Co occupancies. The proposed values of U for the $Co^{2+}$ and $Co^{3+}$ ions in the main Co oxides span the 3.5−6.7 eV interval. Quite importantly, the DFT+U energetics of reduction/oxidation reactions is known to depend linearly on the value of this parameter.[17] Here, we compare the accuracy of the water oxidation energetics calculated with DFT and DFT+U against more accurate methods, also in the context of determining appropriate values of the U parameter.

Much less information is available for the Co oxide clusters and nanoparticles that are at the core of the amorphous CoPi materials, which presently lack an established structural model of their complex surfaces. On the basis of X-ray absorption fine structure (EXAFS) spectroscopy, the presence of crystallites comprised of edge-sharing $CO_6$ octahedra and corner- and face-sharing cubane units was proposed.[13,15,18,19] The stability of such interlinked cubane units was also predicted by our recent theoretical work, which, in addition, provided information about the structure of the phosphate groups at the nanoparticle surface.[20] The reaction energies and the O–O bond mechanism catalyzed by cobalt oxide clusters were recently estimated with DFT calculations employing the B3LYP hybrid functional[21] and the DFT+U approach.[22] In this Letter, we demonstrate that the presence of phosphate groups at the surfaces of CoPi catalysts does not affect the thermodynamics of the OER promoted by Co oxide nanoparticles and discuss the general implications of the benchmarking of the DFT simulation for the OER.

*Model Structures of CoO Clusters.* Experimental measurements performed on CoPi show that in these electrodeposited films, most of the Co ions are in oxidation state 3+. The stoichiometry, composition and charge of all models were therefore chosen to yield a formal 3+ oxidation state of all of the Co ions.

Three structural models of Co oxide clusters were used to benchmark the energies calculated for the water oxidation reaction (Figure 1). The first one, which we refer to as the
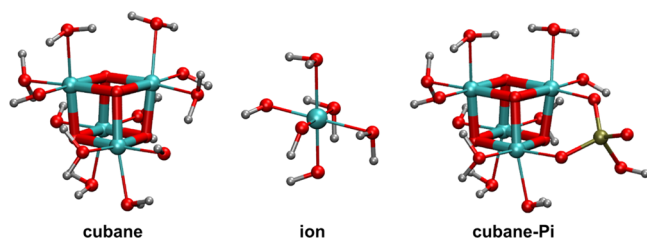


**Figure 1.** Minimal cubane and ion structural models of the active sites of Co oxide nanoparticles. In the cubane-Pi, a surface phosphate group is included so as to determine its effect on the energetics. Co, O, H, and P atoms are represented by blue, red, white, and dark-yellow spheres, respectively.
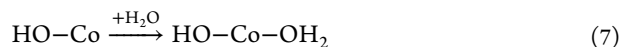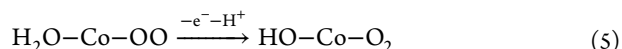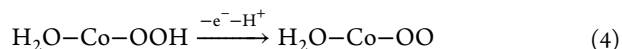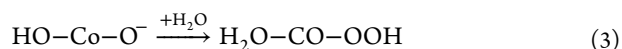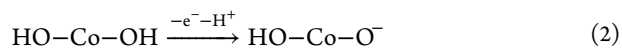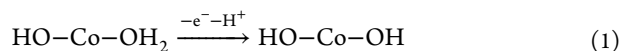
cubane model, is based on a cobalt-oxo $Co_4O_4$ cubane cluster with eight water molecules and four OH groups bound to the Co centers. This model was also at the basis of the QM/MM simulations by Wang and Van Voorhis.[21] The cubic motif is motivated by the models proposed from the EXAFS data[13,15,18] and by the results of our simulations on Co-Pi grains.[20] The latter results demonstrate the local ordering of the catalyst in the form of corner- and face-sharing cubane units. The cubane

model is too big for coupled cluster (CC) calculations, which were performed on a smaller structural model, the ion model. This model consists of one Co center, coordinated by three OH groups, which mimic the Co–O bonds of the cubane, and by three water molecules. The effect of surface phosphate groups on the calculated energies is addressed with the cubane-Pi model, in which two ligands, OH and $H_2O$, of the cubane model are substituted with a phosphate group. The cubane and ion models are neutral, while cubane-Pi has a −1 charge.

*Model Reaction Mechanism.* The water oxidation is a four-electron/four-proton electrochemical reaction that leads to the formation of molecular $O_2$

$$2H_2O \rightarrow 4e^- + 4H^+ + O_2$$
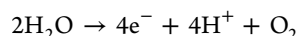
Predicting the water oxidation reaction mechanism catalyzed by Co oxide clusters is not the goal of this Letter. The aim of this work is to compare the energies of water oxidation at different levels of theory. In order to make consistent comparisons, we will employ a well-defined sequence of reaction steps that have previously been proposed for OER catalysts.[6,16,23] The model reaction mechanism is displayed in Figure 2. It involves one metal center, which we assume to be in oxidation state 3+, surrounded by a OH and two $H_2O$ ligands. The individual reaction steps in terms of the change in ligands at one Co site are as follows (see also Figure 2):

$$HO-Co-OH_2 \xrightarrow{-e^- -H^+} HO-Co-OH \quad (1)$$

$$HO-Co-OH \xrightarrow{-e^- -H^+} HO-Co-O^- \quad (2)$$

$$HO-Co-O^- \xrightarrow{+H_2O} H_2O-CO-OOH \quad (3)$$

$$H_2O-Co-OOH \xrightarrow{-e^- -H^+} H_2O-Co-OO \quad (4)$$

$$H_2O-Co-OO \xrightarrow{-e^- -H^+} HO-Co-O_2 \quad (5)$$

$$HO-Co-O_2 \xrightarrow{-O_2} HO-Co \quad (6)$$

$$HO-Co \xrightarrow{+H_2O} HO-Co-OH_2 \quad (7)$$

The first two proton-coupled electron transfer (PCET) steps (eqs 1 and 2) lead to the formation of a $Co-O^-$ group containing an oxyl radical. The third step (eq 3) is the nucleophilic attack of a solvent molecule on this $Co-O^-$ species, which yields a hydroperoxo $Co-OOH$ group and the key O–O bond. The next two PCET steps lead to a superoxo (eq 4) and molecular $O_2$ (eq 5) groups. Oxygen is then evolved in eq 6, and the catalyst is regenerated when a solvent water molecule bonds to the Co site in the final step (eq 7). We stress that this is just one of the many possible water oxidation paths
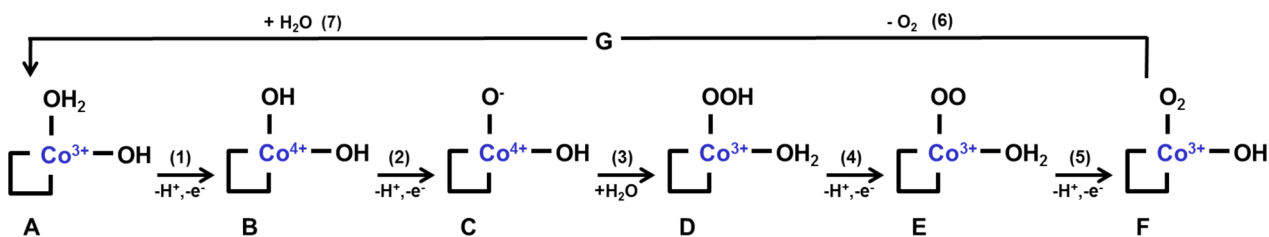


**Figure 2.** Schematic representation of the model reaction mechanism used to compare the different theoretical approaches. The numbers labeling the PCET steps refer to the corresponding equations displayed in the text.
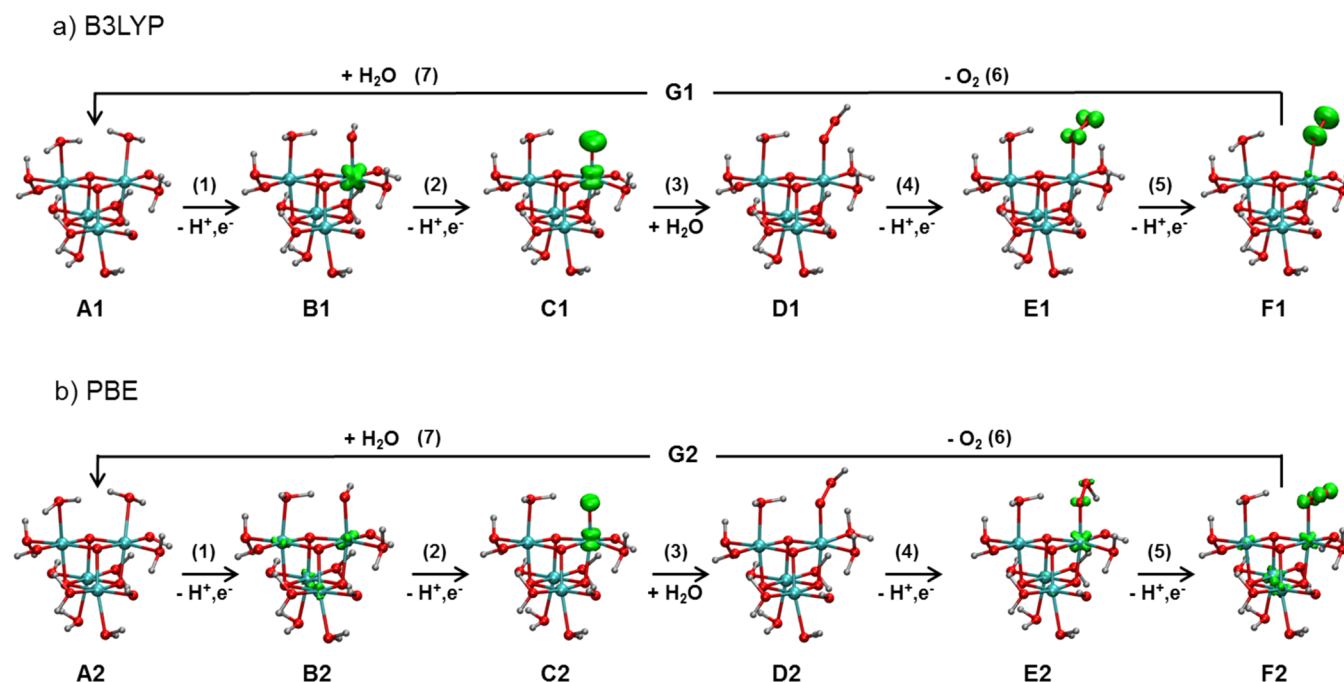
a) B3LYP



b) PBE



**Figure 3.** B3LYP and PBE optimized structures along the reaction pathway for the cubane model. Intermediates are labeled according to the reaction scheme shown in Figure 2. Co, O, and H atoms are represented by blue, red, and white spheres, respectively. Green isosurfaces show the spin density distribution and are plotted for an isovalue of 0.05 Å$^{-3}$.

available at cobalt oxide surfaces, though not necessarily the path of lowest energy.

*Atomic and Electronic Structures: Cubane Model.* Figure 3 shows the optimized geometries of the cubane model obtained with the B3LYP and GGA-PBE functionals along the reaction pathway (eqs 1−7). The spin density is also shown for all open-shell systems and is represented by green isosurfaces. The atomic and electronic structures obtained with the PBE0 functional are very similar to the B3LYP results; therefore, they are discussed together. The main bond lengths at the reaction site are reported in Table 1.

In the initial state of the cubane model (panels A1/A2 in Figure 3), each Co ion is in an octahedral site formed by three O ions of the lattice, two O atoms of the $H_2O$ molecules, and

**Table 1. Co−O and O−O Bond Distances (in Å) for the Reaction Intermediates (A−F) Calculated with Different Functionals for Three Structural Models[a]**

| | | cubane | | | cubane-Pi | | ion |
|---|---|---|---|---|---|---|---|
| | | | | | NN | NNN | |
| | bond | PBE | PBE0 | B3LYP | B3LYP | | B3LYP |
| A | Co−OH$_2$ | 2.04 | 2.00 | 2.03 | 2.07 | 2.05 | 2.01 |
| B | Co−OH | 1.89 | 1.83 | 1.84 | 1.82 | 1.85 | 1.79 |
| C | Co−O | 1.68 | 1.67 | 1.65 | 1.65 | 1.65 | 1.66 |
| D | Co−OOH | 1.88 | 1.90 | 1.92 | 1.87 | 1.93 | 1.86 |
| | O−OH | 1.54 | 1.45 | 1.48 | 1.46 | 1.48 | 1.46 |
| E | Co−OO | 1.83 | 1.90 | 1.92 | 1.92 | 1.92 | 1.90 |
| | O−O | 1.43 | 1.30 | 1.32 | 1.32 | 1.32 | 1.31 |
| F | Co−O$_2$ | 1.86 | 2.14 | 2.07 | 2.06 | 2.00 | 2.24 |
| | O−O | 1.32 | 1.19 | 1.21 | 1.22 | 1.22 | 1.21 |

[a]NN and NNN labels refer to the position of the phosphate group with respect to the active cobalt center: NN, nearest neighbor; NNN, next nearest neighbor.

one O atom of the OH ligands. On the basis of the calculated electronic structure and population analysis (see Tables S1 and S2 in the Supporting Information), we can associate the metal centers in the initial states to low-spin $Co^{3+}$ ions.

The first PCET step (eq 1) converts one of the Co−OH$_2$ moieties into Co−OH (panels B1 and B2 in Figure 3). As expected, the hybrid functionals predict that the unpaired electron resulting from the oxidation of $Co^{3+}$ to $Co^{4+}$ is fully localized on one Co site (green isosurface in B1 in Figure 3). However, the electronic structure obtained with PBE-GGA functional shows delocalization of the spin density over four metal ions (B2 in Figure 3).

Both the hybrid and GGA functionals provide a qualitatively equivalent description of the second PCET step (eq 2), leading to the formation of a Co−O moiety that can be assigned to $Co^{4+}$-oxyl species (panels C1 and C2 in Figure 3). All of the calculations predict the triplet spin state for this structure. The Mulliken population analysis indicates localization of one electron on the $Co^{4+}$ and another on the $O^-$ site (see Tables S1 and S2 in the Supporting Information).

An important structural difference can be seen in the Co−OOH product of water addition to the Co−O group (eq 3). The B3LYP and PBE0 functionals predict the formation of a hydroperoxo Co−OOH group (panel D1 in Figure 3), as indicated by the fact that the O−O bond length is characteristic of a peroxo species (1.45−1.48 Å, Table 1), whereas PBE-GGA leads to a partially formed peroxo group, with a much longer O−O bond (1.54 Å).

The major discrepancy between the hybrid and GGA results is found in the electronic and structural responses to the two PCET steps shown in eq 4 and 5. The B3LYP and PBE0 functionals predict that the peroxo group in the $H_2O$−Co−OOH moiety will first oxidize to a superoxo $H_2O$−Co−OO (panel E1 in Figure 3), as indicated by the localization of the spin density on the O−O ligand and by the O−O bond length

(1.30−1.32 Å, Table 1). The next PCET step leads to the formation of a hydroxo ligand neighboring the superoxo group (HO−Co−OO, panel F1 in Figure 3). The PBE functional inverts this order and predicts first the formation of the hydroxo group in the HO−Co−OOH moiety (panel E2 in Figure 3) and then the formation of the superoxo group (panel F2 in Figure 3). Note that we removed the proton from the Co−OOH group of intermediate D2 in Figure 3, but the resulting $H_2O$−Co−OO moiety is not stable in GGA-PBE because a H atom spontaneously transfers from the neighboring water ligand and forms the HO−Co−OOH E2 intermediate in Figure 3. We also call the readers attention to the different localization of the spin density at steps (4) and (5) in Figure 3 for the individual functionals.

Finally, the product of step (5) (panel F in Figure 3) is a bound molecular $O_2$ in the case of B3LYP/PBE0 (the O−O bond length is 1.21/1.19 Å, Table 1), while it is a bound superoxide $O_2^-$ in the case of GGA-PBE (the O−O bond length is 1.32 Å).

These differences have important implications on the energetics of the cycle, which will be discussed in the following.

*Reaction Energetics for the Cubane Model.* The qualitative structural differences between the functionals described above are reflected in the calculated reaction free energies (see Figure 4). Overall, the B3LYP and PBE0 functionals yield similar
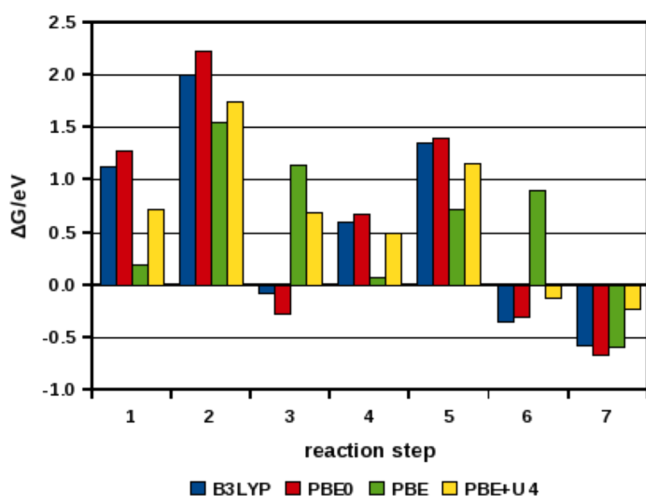


**Figure 4.** Reaction free energies for the cubane model obtained with B3LYP, PBE0, PBE+U (U = 4 eV), and PBE functionals. The corresponding numbers are reported in the Supporting Information, Table S3.

results, as shown by the blue and red histograms, respectively. The largest difference is associated with the formation of the oxo ligand (0.22 eV, around 10%). Among the PCET steps, the largest $\Delta G$ is required for the formation of the Co−O species (step (2) in Figure 3, 2.00/2.22 eV for B3LYP/PBE0, respectively), followed by the formation of molecular $O_2$ (step (5), 1.35/1.40 eV), the hydroxo (step (1), 1.13/1.27 eV), and the superoxo (step (4), 0.60/0.67 eV) ligands. The addition of water (steps (3) and (7) in Figure 3) and the desorption of molecular oxygen from the Co site (step (6)) can be seen to be exothermic.

The energies computed with the PBE-GGA functional (green histograms in Figure 4) differ substantially from those obtained using the hybrid functionals, though the most demanding electrochemical step is still the formation of the Co−O ligand. Similar observations were reported for water oxidation by Ru oxide clusters.[24,25] As described above, the formation of the hydroperoxo in PBE follows a qualitatively different pathway than that in B3LYP/PBE0. This difference explains the major discrepancy in the calculated energies of step (3) in Figure 3, which disagree with the hybrid result even in the sign of the free energy. The other main difference is associated with the desorption of $O_2$ (eq 6), which for PBE is very endothermic ($\Delta G = 0.90$ eV) while it is exothermic for the hybrid functionals (−0.34/−0.30 eV for B3LYP/PBE0, respectively). This is due to the aforementioned different structure of the O−O unit in intermediates F1 and F2 in Figure 3. PBE calculations (panel F2 in Figure 3) describe it as a superoxo species, while the hybrid calculations describe it as molecular oxygen in a triplet spin state. Obviously, the desorption of the latter is much easier compared to a superoxo species, where additional electron transfer from the $O_2$ unit to the metal center has to occur.

Given the substantial discrepancies that we found using the different DFT functionals, we examine the energetics of the same reaction steps with higher-level quantum chemistry methods, in an effort to benchmark the accuracy of the various functionals. However, due to the high computational cost of these calculations, the benchmarking is done on the smaller ion model.

*Ion Model: DFT Results.* The B3LYP optimized geometries along the reaction pathway for the ion model are shown in Figure 5. The optimized distances between the metal center and the ligands for all of the intermediates are in good agreement with those calculated for the cubane model (Table 1). The average difference between the bond lengths in the two models is 0.04 Å. Surprisingly, the B3LYP and PBE0 reaction energies are also in fair agreement with those obtained using the cubane model (Figure 6). As an example, the reaction free
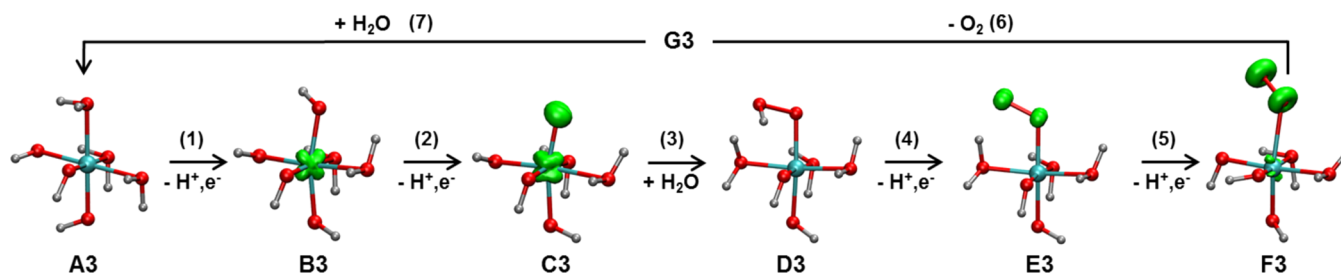


**Figure 5.** B3LYP optimized structures along the reaction pathway for the ion model. Intermediates are labeled according to the reaction scheme shown in Figure 2. Co, O, and H atoms are represented by blue, red, and white spheres, respectively. Green isosurfaces show the spin density distribution and are plotted for an isovalue of 0.05 Å$^{-3}$.
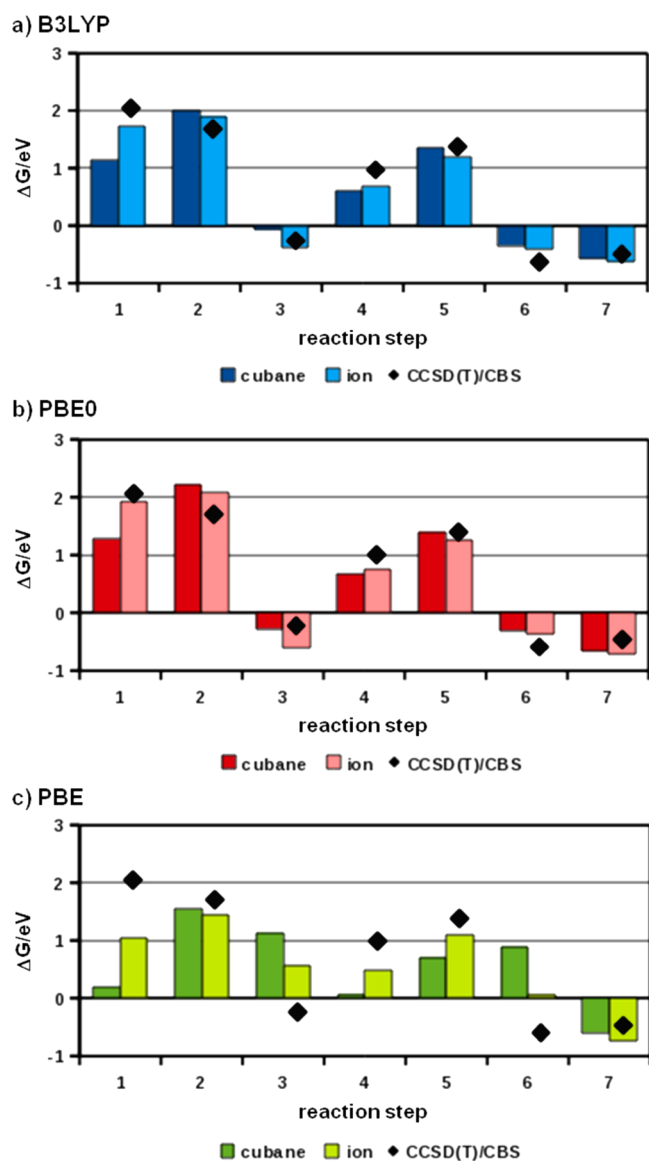
a) B3LYP



b) PBE0



c) PBE



**Figure 6.** Comparison of reaction free energies between the cubane and ion models for (a) B3LYP, (b) PBE0, and (c) PBE functionals. Additionally, our best estimate and reference given by CCSD(T)/CBS are reported. The corresponding numbers are reported in the Supporting Information, Table S4.

energy of the overpotential limiting step for the ion and cubane models differs by only 0.09 and 0.14 eV for the B3LYP and PBE0 calculations, respectively. This observation suggests that

the ion model mimics the main features of the active site and is therefore a reasonable system for benchmarking.

Also for the ionic model, the PBE-GGA energies are still far from the B3LYP/PBE0 results, although the discrepancies are systematically smaller. This apparent better agreement is an artifact of the presence of just one metal center, which forces the hole to localize on the Co site in the PBE calculations.

*Ion Model: MP2 and CCSD(T) Results.* Before comparing our DFT results to higher-level calculations, one needs to ensure that all of the species involved in the mechanism are well-described with a single reference wave function. For this reason, the T1 diagnostic is evaluated (within the CC calculations) for each intermediate along the reaction pathway (see Table S5 and the T1 diagnostic section in the Supporting Information). Our results indicate significant multireference character of intermediate **C**; therefore, we need to keep in mind that the MP and CC energies are not reliable in this case.

Table S4 (Supporting Information) reports the reaction free energies obtained with the MP and CC methods as single-point calculations on the optimized B3LYP structures (with the same 6-311G** basis set). We have performed a full set of MP calculations (MP2, MP3, MP4(DQ), and MP4(SDQ)) that however show important differences between them and large deviations from the CCSD(T) reference, particularly for the first three reaction steps. The CCSD and MP4(SDQ) values do not agree, which indicates that the MP series is not converged at fourth order. Therefore, we will focus on the CC results. The CCSD(T) energies are usually slightly lower than the CCSD and closer to the DFT results with hybrid functionals. This fact indicates the importance of the triples contribution for treatment of correlation.

Because the DFT results converge faster than MP and CC calculations as a function of the basis set size, we employed the extrapolation to the complete basis set (CBS) for these latter methods (Table 2). The extrapolation is done using only double- and triple-ζ basis sets (from the cc-pVXZ family)[26] due to the cost of the calculations; therefore, it is rather an estimation of the CBS limit value.

We find that the reaction energies usually increase as a function of the basis set completeness. The largest difference between the double- and triple-ζ basis set is for reaction steps (2) and (3), in which structure **C** takes part, confirming the multireference character of this intermediate. Our best estimate and reference in this analysis are given by the CCSD(T)/CBS approach, whose energies are shown in Figure 6 with a black diamond symbol. It is evident that the hybrid functionals give comparable results to the CCSD(T)/CBS ones.

Figure 7 displays the differences between the CCSD(T)/ CBS reaction free energies and the corresponding PBE, PBE0,

**Table 2. MP and CC Reaction Energies (in eV) Obtained Using Correlation-Consistent Basis Sets and Extrapolation to the CBS Limit**

| | MP2 | | | MP4(SDQ) | | | CCSD | | | CCSD(T) | | |
|---|---|---|---|---|---|---|---|---|---|---|---|---|
| step | pVDZ | pVTZ | CBS | pVDZ | pVTZ | CBS | pVDZ | pVTZ | CBS | pVDZ | pVTZ | CBS |
| (1) **A → B** | 1.64 | 1.79 | 1.84 | 1.68 | 1.77 | 1.82 | 2.75 | 2.88 | 2.98 | 2.28 | 2.36 | 2.43 |
| (2) **B → C** | 2.49 | 5.58 | 7.40 | 1.86 | 5.00 | 6.84 | 2.17 | 2.37 | 2.97 | 2.01 | 1.66 | 2.04 |
| (3) **C → D** | −0.79 | −3.77 | −5.65 | −0.22 | −3.20 | −5.07 | −1.66 | −1.77 | −2.39 | −1.14 | −0.62 | −1.02 |
| (4) **D → E** | 1.43 | 1.59 | 1.67 | 1.27 | 1.38 | 1.44 | 1.18 | 1.30 | 1.36 | 1.15 | 1.29 | 1.36 |
| (5) **E → F** | 1.62 | 1.87 | 2.01 | 1.63 | 1.84 | 1.96 | 1.48 | 1.65 | 1.74 | 1.51 | 1.70 | 1.80 |
| (6) **F → G** | −0.26 | −0.43 | −0.47 | −0.25 | −0.42 | −0.46 | 0.14 | −0.02 | −0.04 | 0.17 | 0.00 | −0.04 |
| (7) **G → A** | −1.38 | −1.22 | −1.23 | −1.27 | −1.12 | −1.12 | −1.35 | −1.18 | −1.18 | −1.36 | −1.20 | −1.20 |
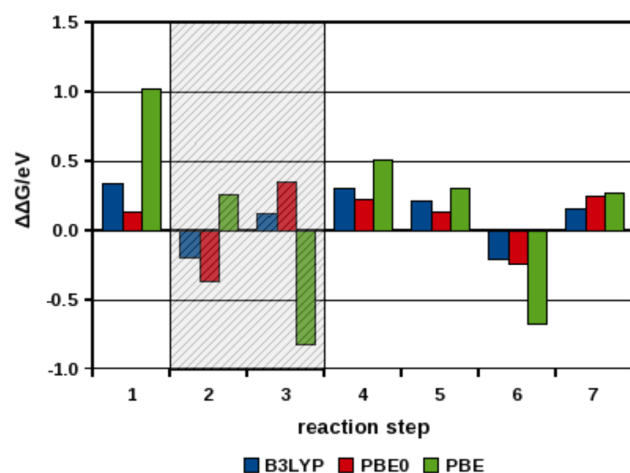
**Figure 7.** Differences in reaction free energies between DFT functionals and CCSD(T)/CBS results. The corresponding numbers are reported in the Supporting Information, Table S6.



**Figure 8.** The energy cost for the first reaction step obtained with PBE+U (U = 0−7 eV) compared with B3LYP and PBE0 results.

and B3LYP results. Steps (2) and (3) are excluded from this analysis due to the multireference character of the intermediate **C** (shaded area). Both the PBE0 and B3LYP results are in good agreement with the reference CCSD(T)/CBS values. The average error in the PCET steps is smaller for PBE0 compared to that for B3LYP (0.17 and 0.29 eV, respectively).

*PBE+U Approach.* Including a model description of the on-site Coulomb repulsion in DFT functionals (DFT+U) is a practical way to cope with the problem of electronic self-interaction, which is not properly canceled out by the standard LDA and GGA functionals. The DFT+U approach has been shown to correctly reproduce the insulating character and the charge localization of several transition-metal oxides, which were incorrectly described by the plain functionals. In particular, we note that the value of the U parameter has a pivotal role in the calculation of reaction energies involving Co oxidation or reduction. As an example, the DFT+U oxidation energy of CoO to $Co_3O_4$ changes by 8 eV in the U = 0−6 eV interval.[17]

Chen and Selloni have applied the DFT+U method to describe the structural and electronic properties of $Co_3O_4$ bulk and surfaces and have calculated U values of 4.4 (for $Co^{3+}$) and 6.7 eV (for $Co^{2+}$) with the linear response method.[4] The average, U = 5.9 eV, was then used in their surface science analysis, including the reaction energies for water oxidation.[6] A much smaller value, U = 3.52 eV, was proposed by Garcia-Mota and co-workers on the basis of the calculated $CoO−Co_3O_4$ thermodynamics. DFT+U calculations with this value of U were used to study the activity of Co oxides for the electrochemical water oxidation.[8] Given this broad interval of proposed values and the strong U dependency of the DFT+U energies, it is valuable to benchmark the accuracy of this method against high-level quantum chemistry data.

Figure 8 displays the reaction free energy of the first PCET step of our model reaction (eq 1) for the cubane model, as a function of the U parameter. The corresponding B3LYP and PBE0 values are shown with dashed horizontal lines. The overall agreement between the PBE+U and the hybrid calculations increases considerably in the interval U = [0,4] eV and remains approximately constant for U between 4 and 7 eV. For U = 4 eV, the difference with the B3LYP value is 0.41 eV (36%). The same level of accuracy is also shown for the ion
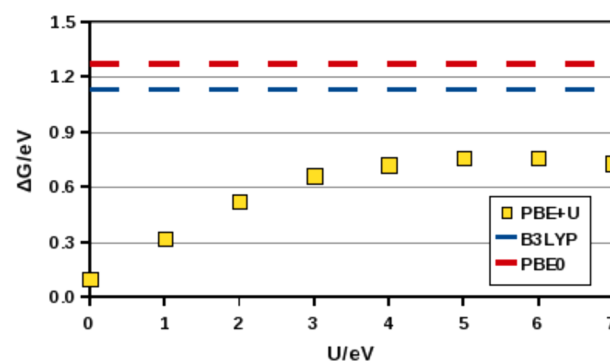
model, where the PBE+U energies differ by 0.37 eV from the B3LYP and 0.71 eV from the CC values.

The PBE+U reaction energies with U = 4 eV along the whole reaction pathway are compared to the PBE and hybrid results in Figure 4. Besides improving the description of hole localization during oxidation, it is evident that the PBE+U approach predicts reaction energetics that are in much better agreement with the hybrid functional and CC results than the PBE data. The average discrepancy of the PBE+U and PBE results with respect to the B3LYP values is 0.25 and 0.70 eV, respectively. Quite importantly, we conclude that, at least for this specific case of a minimal cubane nanoparticle, it is not possible to find a specific value of U that reproduces the reference CC energies. This issue and its extension to oxide surfaces is the subject of ongoing work that will be reported separately.

*Effect of Phosphate Surface Groups on Thermodynamics.* There is very little available information on the position and role of the phosphate groups in the CoPi catalysts described in the introduction. Our previous study predicted equilibrium geometries of these groups at the surface of the CoPi nano-particles.[20] Here, we investigate whether the presence of these surface groups affects the thermodynamics of water oxidation promoted by the Co oxide terminations of the catalyst. To this end, we employed the cubane-Pi model with a bidentate phosphate group bridging across the diagonal of the cubane facet. We considered two different positions of the $PO_4$ group, nearest neighbor (NN, shown in Figure 1) and next nearest neighbor (NNN), with respect to the active cobalt center.

The reaction free energies calculated at the B3LYP level in the presence (cubane-Pi) and absence (cubane) of a surface phosphate group are reported in Figure 9. These calculations clearly show that the phosphate groups at the surface of the CoPi nanoparticles do not affect the thermodynamics of the OER, regardless of the position of the phosphate with respect to the active Co center. The small changes in relative energies (see Table S8 in the Supporting Information) are caused mostly by different H bonding around the cube moiety (see Figure S1, Supporting Information).

In conclusion, ab initio DFT simulations are routinely used to provide key insight into the reaction mechanism and thermodynamics of the OER promoted by reducible transition-metal oxides. The accuracy of these simulations relies on several approximations, most relevantly relating to the electronic structure of the catalyst and to the energetics of the electrochemical steps. Experimental data can be readily used to evaluate the accuracy of the calculated electronic and
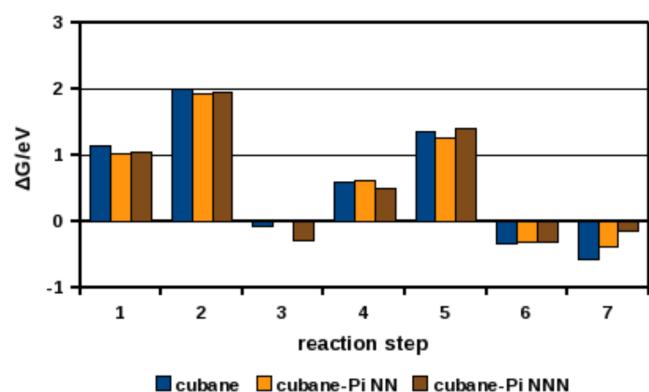
**Figure 9.** B3LYP reaction free energies for the cubane and cubane-Pi models. The corresponding numbers are reported in the Supporting Information, Table S8.

structural properties, that is, for materials characterization. Assessing the accuracy of the thermodynamics calculated for electrochemical reactions is problematic, both because experimental data on individual reaction steps is often unavailable and because of the inherent assumptions required to calculate such energies. In this work, we separate the effects of these latter assumptions on the calculated energies from the effects of the approximations used to describe the electronic structure.

Our CC calculations provide a highly accurate computational estimate of the OER thermodynamics for a realistic model reaction pathway and active site of cobalt oxide nanoparticles. This study demonstrates that hybrid B3LYP and PBE0 functionals can adequately reproduce the CC reference energies, while plain GGA calculations lead to very important discrepancies.

The OER mechanistic studies promoted by Co oxide surfaces and clusters available so far have mostly employed the PBE+U approach.[6,8,16,22] We show that the inclusion of a model Hubbard U term to the GGA functional substantially improves the GGA energies. However, there is no value of the U parameter that can lead to the same level of general agreement obtained with hybrid functionals. The DFT+U method can therefore be a viable approach for the effective large-scale simulation of cobalt oxide catalysts, but the discrepancies in the predicted energetics should be taken into account. We show that the DFT+U reaction energies are weakly dependent on the value of U in the interval of U = 4−7 eV. This observation can be used to rationalize the very different values of U employed in DFT+U simulations of cobalt oxides when studying water oxidation.

Finally, our calculations show that the phosphate groups present at the surface of CoPi nanoparticles do not change the thermodynamics of the OER promoted by these catalysts. The surface Co ions exposed to the solvent promote water oxidation and $O_2$ evolution independent of the presence of neighboring phosphate groups. The possible importance of these species in the dynamic processes at the surface/solvent interface is presently under analysis.

### ■ COMPUTATIONAL METHODS

We have performed DFT calculations employing different approximations for the exchange−correlation (XC) functional. In addition, higher-level quantum chemistry calculations were employed to assess the accuracy of the XC approximations against the most accurate coupled cluster method. The calculations were performed considering three structural models (cubane, ion, and cubane-Pi; Figure 1) and a specific prototypical reaction path described in the model reaction discussion.

The DFT calculations with local basis sets were performed with the Gaussian09 pogram[27] using the PBE-GGA,[28] the PBE0,[29] and the B3LYP[30,31] functionals. For the calculations employing the B3LYP functional, all of the reaction intermediates along the reaction path were optimized and confirmed by vibrational analysis to be local minima (for all models). The PBE and PBE0 energetics for the ion model were obtained on the B3LYP geometries, while the atomic coordinates were fully relaxed for the cubane model. The basis set employed for both structural optimizations and single-point calculations was of triple-$\zeta$ quality with polarization functions (6-311G**)[32,33] for all atoms.

The higher-level quantum chemical calculations were performed on the ion model only. The MP2, MP3, MP4(SD), MP4(SDQ), CCSD, and CCSD(T) single-point energies (with the frozen core approximation) were calculated on the optimized B3LYP geometries using the same basis set (6-311G**) as that for relaxation. Additionally, we employed correlation-consistent basis sets (cc-pVXZ, X = D,T)[26] in order to extrapolate the results to the CBS limit, according to the scheme proposed by Halkier and co-workers.[34]

Additionally, plane wave calculations for the cubane model were performed using the Quantum Espresso package.[35] For this type of calculation, the PBE functional[28] was applied together with a Hubbard U correction.[36] We used ultrasoft pseudopotentials with the energy cutoffs of 30 and 300 Ry for the wave functions and the charge density, respectively.

To compute the free-energy cost of the oxidation steps along the catalytic cycle, we employed the protocol proposed by Nørskov and co-workers,[37] where all oxidations are considered to be PCET processes. This approach has been previously applied for water oxidation[23,38,39] and oxygen reduction[37] reactions on metal and metal oxide surfaces, as well as metal complexes.[24,40] A brief summary of the key concepts of this approach is reported in the Supporting Information.

### ■ ASSOCIATED CONTENT

**Ⓢ Supporting Information**

PBE and B3LYP Mulliken charges and spin densities for the cubane model; reaction free energies for the cubane, ion, and cubane-Pi models obtained using different functionals; T1 diagnostic analysis from CCSD(T) calculations for the ion model; comparison of reaction free energies between different DFT functionals and CCSD(T); spin contaminant values for open-shell structures (ion model); and description of the method to compute free-energy changes of electrochemical steps. This material is available free of charge via the Internet at http://pubs.acs.org.

### ■ AUTHOR INFORMATION

**Corresponding Author**

*E-mail: fabris@sissa.it.

**Notes**

The authors declare no competing financial interest.

## ■ REFERENCES

(1) Lewis, N. S.; Nocera, D. G. *Proc. Natl. Acad. Sci. U.S.A.* **2006**, *103*, 15729−15735.

(2) McCool, N. S.; Robinson, D. M.; Sheats, J. E.; Dismukes, G. C. *J. Am. Chem. Soc.* **2011**, *133*, 11446−11449.

(3) Nocera, D. G. *Acc. Chem. Res.* **2012**, *45*, 767−776.

(4) Chen, J.; Wu, X.; Selloni, A. *Phys. Rev. B* **2011**, *83*, 245204.

(5) Chen, J.; Selloni, A. *Phys. Rev. B* **2012**, *85*, 085306.

(6) Chen, J.; Selloni, A. *J. Phys. Chem. Lett.* **2012**, *3*, 2808−2814.

(7) Yusuf, S.; Jiao, F. *ACS Catal.* **2012**, *2*, 2753−2760.

(8) Garcia-Mota, M.; Bajdich, M.; Viswanathan, V.; Bell, A. T.; Nørskov, J. K. *J. Phys. Chem. C* **2012**, *116*, 21077−21082.

(9) Risch, M.; Grimaud, A.; May, K. J.; Stoerzinger, K. A.; Chen, T. J.; Mansour, A. N.; Shao-Horn, Y. *J. Phys. Chem. C* **2013**, *117*, 8628−8635.

(10) Pijpers, J. J. H.; Winkler, M. T.; Surendranath, Y.; Buonassisi, T.; Nocera, D. G. *Proc. Natl. Acad. Sci. U.S.A.* **2011**, *108*, 10056−10061.

(11) Kanan, M. W.; Nocera, D. G. *Science* **2008**, *321*, 1072−1075.

(12) Surendranath, Y.; Dinca, M.; Nocera, D. G. *J. Am. Chem. Soc.* **2009**, *131*, 2615−2620.

(13) Farrow, C. L.; Bediako, D. K.; Surendranath, Y.; Nocera, D. G.; Billinge, S. J. L. *J. Am. Chem. Soc.* **2013**, *135*, 6403−6406.

(14) Surendranath, Y.; Lutterman, D. A.; Liu, Y.; Nocera, D. G. *J. Am. Chem. Soc.* **2012**, *134*, 6326−6336.

(15) Surendranath, Y.; Kanan, M. W.; Nocera, D. G. *J. Am. Chem. Soc.* **2010**, *132*, 16501−16509.

(16) Bajdich, M.; Garcia-Mota, M.; Vojvodic, A.; Nørskov, J. K.; Bell, A. T. *J. Am. Chem. Soc.* **2013**, *135*, 13521−13530.

(17) Wang, L.; Maxisch, T.; Ceder, G. *Phys. Rev. B* **2006**, *73*, 195107.

(18) Risch, M.; Klingan, K.; Ringleb, F.; Chernev, P.; Zaharieva, I.; Fischer, A.; Dau, H. *ChemSusChem* **2012**, *5*, 542−549.

(19) Mattioli, G.; Risch, M.; Bonapasta, A. A.; Dau, H.; Guidoni, L. *Phys. Chem. Chem. Phys.* **2011**, *13*, 15437−15441.

(20) Hu, X. L.; Piccinin, S.; Laio, A.; Fabris, S. *ACS Nano* **2012**, *6*, 10497−10504.

(21) Wang, L.-P.; Van Voorhis, T. *J. Phys. Chem. Lett.* **2011**, *2*, 2200−2204.

(22) Mattioli, G.; Giannozzi, P.; Bonapasta, A. A.; Guidoni, L. *J. Am. Chem. Soc.* **2013**, *135*, 15353−15363.

(23) Rossmeisl, J.; Qu, Z. W.; Zhu, H.; Kroes, G. J.; Nørskov, J. K. *J. Electroanal. Chem.* **2007**, *607*, 83−89.

(24) Piccinin, S.; Fabris, S. *Phys. Chem. Chem. Phys.* **2011**, *13*, 7666−7674.

(25) Piccinin, S.; Sartorel, A.; Aquilanti, G.; Goldoni, A.; Bonchio, M.; Fabris, S. *Proc. Natl. Acad. Sci. U.S.A.* **2013**, *110*, 4917−4922.

(26) Dunning, T. H., Jr. *J. Chem. Phys.* **1989**, *90*, 1007.

(27) Frisch, M. J.; et al. *Gaussian 09*, revision A.1; Gaussian Inc.: Wallingford, CT, 2009.

(28) Perdew, J. P.; Burke, K.; Ernzerhof, M. *Phys. Rev. Lett.* **1996**, *77*, 3865.

(29) Perdew, J. P.; Burke, K.; Ernzerhof, M. *J. Chem. Phys.* **1996**, *105*, 9982.

(30) Becke, A. D. *J. Chem. Phys.* **1998**, *98*, 5648.

(31) Lee, C.; Yang, W.; Parr, R. G. *Phys. Rev. B* **1998**, *37*, 785.

(32) Krishnan, R.; Binkley, J. S.; Seeger, R.; Pople, J. A. *J. Chem. Phys.* **1980**, *72*, 650.

(33) Francl, M. M.; Pietro, W. J.; Hehre, W. J.; Binkley, J. S.; Gordon, M. S.; DeFrees, D. J.; Pople, J. A. *J. Chem. Phys.* **1982**, *77*, 3654.

(34) Halkier, A.; Helgaker, T.; Jørgensen, P.; Klopper, W.; Koch, H.; Olsen, J.; Wilson, A. K. *Chem. Phys. Lett.* **1998**, *286*, 243−252.

(35) Giannozzi, P.; et al. *J. Phys.: Condens. Matter.* **2009**, *21*, 395502.

(36) Anisimov, V. I.; Zaanen, J.; Andersen, O. K. *Phys. Rev. B* **1991**, *44*, 943−954.

(37) Nørskov, J. K.; Rossmeisl, J.; Logadottir, A.; Lindqvist, L.; Kitchin, J. R.; Bligaard, T.; Jónsson, H. *J. Phys. Chem. B* **2004**, *108*, 17886−17892.

(38) Rossmeisl, J.; Logadottir, A.; Nørskov, J. K. *Chem. Phys.* **2005**, *319*, 178−184.

(39) Rossmeisl, J.; Nørskov, J. K.; Taylor, C. D.; Janik, M. J.; Neurock, M. *J. Phys. Chem. B* **2006**, *110*, 21833−21839.

(40) Mayer, J. M. *Annu. Rev. Phys. Chem.* **2004**, *55*, 363−390.